Elsevier Editorial System(tm) for
International Journal of Hydrogen Energy
Manuscript Draft

Manuscript Number: HE-D-19-02304R1

Title: Microkinetic modelling and reaction pathway analysis of the steam reforming of ethanol over Ni/SiO2

Article Type: Full Length Article

Section/Category: Chemical, Thermochemical & Electrochemical Hydrogen

Keywords: Ethanol steam reforming; Nickel catalyst; Microkinetic modelling

Corresponding Author: Dr. Panagiotis Kechagiopoulos,

Corresponding Author's Institution: University of Aberdeen

First Author: Ahmed Tijani Afolabi

Order of Authors: Ahmed Tijani Afolabi; Chun-Zhu Li; Panagiotis Kechagiopoulos

Abstract: Hydrogen production via the steam reforming of biomass-derived ethanol is a promising environmental alternative to the use of fossil fuels and a means of clean power generation. A microkinetic modelling study of ethanol steam reforming (ESR) on Nickel is presented for the first time and validated with minimal parameter fitting against experimental data collected over a Ni/SiO2 catalyst. The thermodynamically consistent model utilises Transition State Theory and the UBI-QEP method for the determination of kinetic parameters and is able to describe correctly experimental trends across a wide range of conditions. The kinetically controlling reaction steps are predicted to occur in the dehydrogenation pathway of ethanol, with the latter found to proceed primarily via the formation of 1-hydroxyethyl. C-C bond cleavage is predicted to take place at the ketene intermediate leading to the formation of CH2 and CO surface species. The latter intermediates proceed to react according to methane steam reforming and water gas shift pathways that are enhanced by the presence of water derived OH species. The experimentally observed negative reaction order for water is explained by the model predictions via surface saturation effects of adsorbed water species. The model results highlight a possible distinction between ethanol decomposition pathways as predicted by DFT calculations on Ni close-packed surfaces and ethanol steam reforming pathways at the broad range of experimental conditions considered.

Research Data Related to this Submission

There are no linked research data sets for this submission. The following reason is given:
Data will be made available on request

Graphical Abstract (for review)

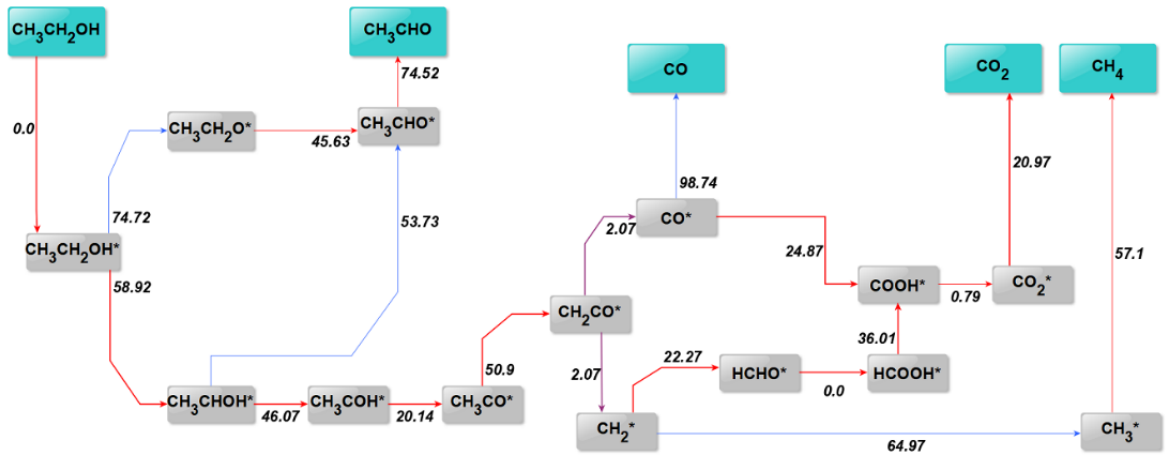

Highlights

- Microkinetic model proposed for ethanol steam reforming over a Ni/SiO_2 catalyst.
- Ni metal driven reaction pathways and observed partial reaction orders explained.
- Ethanol dehydrogenation to 1-hydroxyethyl found rate determining.
- Negative reaction order for water due to surface saturation by adsorbed water.
- Model forms basis for the incorporation of support effects in microkinetics.

Microkinetic modelling and reaction pathway analysis of the steam reforming of ethanol over Ni/SiO_2

Ahmed Tijani F. Afolabi,[1,2] Chun-Zhu Li,[2] Panagiotis N. Kechagiopoulos[1]*

[1]Chemical and Materials Engineering Group, School of Engineering, University of Aberdeen, Aberdeen, AB24 3UE, UK

[2]Fuels and Energy Technology Institute, Curtin University, GPO Box U1987, Perth, WA 6845, Australia

* Corresponding author: p.kechagiopoulos@abdn.ac.uk, +44 (0) 1224 272205

Abstract

Hydrogen production via the steam reforming of biomass-derived ethanol is a promising environmental alternative to the use of fossil fuels and a means of clean power generation. A microkinetic modelling study of ethanol steam reforming (ESR) on Nickel is presented for the first time and validated with minimal parameter fitting against experimental data collected over a Ni/SiO_2 catalyst. The thermodynamically consistent model utilises Transition State Theory and the UBI-QEP method for the determination of kinetic parameters and is able to describe correctly experimental trends across a wide range of conditions. The kinetically controlling reaction steps are predicted to occur in the dehydrogenation pathway of ethanol, with the latter found to proceed primarily via the formation of 1-hydroxyethyl. C-C bond cleavage is predicted to take place at the ketene intermediate leading to the formation of CH_2 and CO surface species. The latter intermediates proceed to react according to methane steam reforming and water gas shift pathways that are enhanced by the presence of water derived OH species. The experimentally observed negative reaction order for water is explained by the model predictions via surface saturation effects of adsorbed water species. The model results highlight a possible distinction between ethanol decomposition pathways as predicted by DFT calculations on Ni close-packed surfaces and ethanol steam reforming pathways at the broad range of experimental conditions considered.

Keywords: Ethanol steam reforming; Nickel catalyst; Microkinetic modelling

1. Introduction

Hydrogen production via steam reforming is of significant research interest due to the potential of hydrogen as an alternative, efficient and environmentally benign energy carrier. Conventional steam reforming of natural gas, however, is accompanied by high CO_2 emissions, both generated as by-product in the reaction stage and follow-up purification, and due to the high heat supply requirements of the process. The utilisation of renewable, biomass-derived, feeds provides the possibility to lower significantly the environmental impact of hydrogen production via steam reforming.

Ethanol steam reforming has been researched extensively, due to its obtainability from the fermentation process of various renewable sources [1–3] and also as a model compound for the lumped alcohol class of the aqueous phase of bio-oil (the liquid product of biomass pyrolysis) [4–6]. The general consensus is that the reaction mechanism primarily depends on the metal catalyst, which facilitates the scission of C-C and C-H bonds [3,7,8]. The support, if active, may participate in the water-gas shift reaction or dehydration of ethanol to ethylene [8], the latter recognised as an important coke precursor, although bifunctional mechanisms with sites at the metal-support interface determining the reaction rate have also been postulated [9]. An extensive understanding of the underlying chemical kinetics as well as the exact role of the metal catalyst is a key to enhancing catalyst performance, as the overall process comprises various sub-mechanisms. The most relevant of these are ethanol dehydrogenation and decomposition, water-gas shift and methane steam reforming/methanation, with maximum hydrogen yield being achieved via the overall ethanol steam reforming reaction, shown in respective order below:

$$C_2H_5OH \rightleftarrows C_2H_4O + H_2 \rightarrow CH_4 + CO + H_2 \quad (1)$$

$$CO + H_2O \rightleftarrows CO_2 + H_2 \quad (2)$$

$$CH_4 + H_2O \rightleftarrows CO + 3H_2 \quad (3)$$

$$C_2H_5OH + 3H_2O \rightleftarrows 2CO_2 + 6H_2 \quad (4)$$

Various theoretical and experimental methods have been applied with the aim of obtaining information on the intrinsic kinetics of the process and clarifying the dominant pathways on various catalysts, including Ni [10–13], Pt [14,15], Rh [10] and Pd [16]. Early on, the isotopic work by Gates et al. [17] proposed that on Ni(111) ethanol decomposition proceeds initially via a O-H bond cleavage leading to the formation of ethoxy species. Following a C-H bond scission the latter species were suggested to dehydrogenate to acetaldehyde, eventually leading to the formation of CH_4 and CO through C-C bond cleavage, with the C-O bond remaining intact. More recently, Wang et al. [10] proposed via DFT calculations a similar pathway for a variety of (111) metal surfaces, including Ni, however ethanol decomposition was primarily identified to occur via CH_2CH_2OH and CH_2CH_2O doubly adsorbed surface intermediates. Ferrin et al. [18] mapped the entire potential energy surface for ethanol decomposition on Pt, Ru, Rh, Pd and Ir using DFT calculations, Brønsted-Evans-Polyani correlations and scaling relations, finding that C-C cleavage in all active surfaces takes place at the ketenyl intermediate. The combined DFT and microkinetics study of ethanol steam reforming on Pt by Sutton et al. [19] agreed with the latter finding, but revealed the first dehydrogenation step to 1-hydroxyethyl as rate limiting. Via periodic DFT calculations Ming Li et al. proposed a similar pathway over Pd [16], however the same authors found an ethoxy based decomposition route to be more probable over Rh [20] with the dehydrogenation of that species being rate-determining. Jia Zhang et al. [21] similarly suggested a pathway via ethoxy on Rh in their DFT study, however C-C scission was predicted to occur at the acetyl intermediate and the water gas shift reaction was identified as rate-controlling. Over Co(0001), the periodic DFT study of Ma et al. [22] attempted to probe the experimental observations and mechanism proposed by Sahoo et al. [23] finding H-abstraction from ethoxy to acetaldehyde to be the rate determining step. The above findings were consolidated in the DFT work on close-packed transition-metal surfaces of Sutton et al. [24] and the review by Zanchet et al. [25]. A dominant finding of these works was that the initial dehydrogenation of ethanol preferentially proceeds via O-H abstraction leading to ethoxy and, eventually, acetaldehyde on Ni, Co and Ru, via α C-H scission on Pt and Pd, and through both pathways on Rh.

It is evident that theoretical studies have focused on the decomposition pathways of ethanol, while all previously reported microkinetic models on ethanol conversion towards syngas are over noble metals, namely Pt [19,26] and Rh [27]. It is recognised though that the high cost of the latter poses significant economic difficulties to the commercial implementation of the process. Ni based catalysts exhibit good activity and are relatively cheap compared to noble metal ones, hence it is particularly important to obtain a mechanistic understanding of ESR on this metal. To this end, in this work a comprehensive microkinetic model for ethanol steam reforming that considers multiple pathways to describe the primary ethanol decomposition and dehydrogenation reactions and the follow-up pathways of their products is proposed and validated using a kinetic dataset collected over a Ni/SiO_2 catalyst at a broad range of experimental conditions [13]. The inert support used aims specifically at the elucidation of the metal-driven reaction pathways, so that support effects can be discerned at a follow-up stage and a unified kinetic view on the ESR mechanism can be obtained.

2. Procedures

2.1. *Experimental details*

The experimental data used in this study have been obtained from the work of Zhurka et al. [13]. Experiments were carried out in a fixed bed reactor setup over a Ni/SiO_2 catalyst under explicit kinetic control. The kinetic dataset obtained covers the effect of temperature, space velocity and partial pressure of reactants across a wide range. A summary of the operating conditions and catalyst properties is provided in Table 1, with more details being available in the original publication.

2.2. *Model formulation and computational details*

The microkinetic model for ethanol stream reforming on Ni catalysts proposed in this work is developed using a FORTRAN based modelling platform, the microkinetic engine (MKE), described in more details previously [28–30]. The experimental data are simulated using a plug flow reactor

model, while the pseudo steady state approximation and a mass balance for the active sites are applied to determine the partial coverage of the surface intermediates. Entropic and enthalpic thermodynamic consistency is upheld by correlating the surface reaction entropies and enthalpies to those of the corresponding gas phase reactions in line with the work of Kechagiopoulos et al. [30]. Surface species entropies are obtained from the equivalent gas species entropies, assuming that upon adsorption all species lose their translational degrees of freedom. Similarly, surface species enthalpies are obtained from the equivalent gas species enthalpies subtracting their chemisorption enthalpies. The temperature dependence of the latter is linked to the degrees of freedom lost or gained upon adsorption or desorption as described in Mhadeshwar et al. [31] and is implemented according to the equation below:

$$Q(T) = Q(T_0) - \gamma R(T - T_0) \tag{5}$$

where γ is the temperature dependence coefficient, R is the universal gas constant and T_0 is taken as 300 K in this study. Modified Arrhenius-type equations and the law of mass action are used to calculate the rates of elementary reactions. For adsorption steps collision theory is used to calculate the maximum values of pre-exponentials factors, the latter further adjusted via sticking coefficients. Pre-exponential factors for forward steps of all reactions involving only surface species are obtained via transition state theory [32]:

$$A_i^f = \left(\frac{k_b T}{h}\right) * \frac{Q_{AB}'''}{Q_A''' Q_B'''}, \qquad where\ Q_i''' = q_{it}''' q_{ir} q_{iv} \tag{6}$$

where k_b is Boltzmann's constant, h is Planck's constant, $Q_i^{'''}$ depicts the overall partition function for a species, with q_{it}''', q_{ir} and q_{iv} depicting the translational, rotational and vibrational partition functions respectively. It is assumed that the ratios of the translational and vibrational partition functions of the transition state and the reactants are approximately unity [19,33], so the molecular partition function ratio is obtained in this work as the ratio of the rotational partition functions of

the transition state and the reactants. These are calculated from the moments of inertia of species I_i as well as the temperature T, as shown below:

$$q_{ir} = \frac{8\pi^2 I_i k_b T}{\sigma h^2} \quad (7)$$

It is further assumed that all species upon adsorption rotate around the vertical axis of the atom attached to the surface of the catalyst. Literature DFT studies are used to discern the most likely adsorption mode for each species [19], while product-like transition states are assumed. The moment of inertia of functional groups with internal rotation or molecules attached to the surface bound atom is calculated based on their bond lengths and angles, while the overall moment of inertia is estimated as the sum of the moment of inertia of all attached groups or atoms rotating around the absorbed atom‘s vertical axis. The pre-exponential factors of reverse reactions for both adsorption and surface reactions are calculated through the preservation of entropic consistency. Adsorption reaction steps are considered non-activated, while the activation barrier for reactions involving surface species are calculated using the UBI-QEP method [34,35]. Activation barriers of reverse reactions are calculated through enthalpic consistency [30]. The Supporting Information provides further details on all related calculations.

The active site density and catalyst surface area were determined experimentally, as reported by Zhurka et al. [13]. The resulting differential and algebraic equations (DAE) system is numerically integrated with the DDASPK solver [36], while to obtain the surface partial coverage at the reactor’s inlet and initialise this DAE system a clean catalyst surface is evolved towards the steady state. Rosenbrock [37] and Levenberg–Marquardt [38,39] optimization methods are used for the estimation of the model’s parameters, namely chemisorption enthalpies, temperature exponents of modified Arrhenius equations and sticking coefficients, through regression of the experimental data, with the objective function being the weighed sum of the squared residuals between the observed and calculated outlet molar flowrates.

2.3. *Surface reaction network description*

A comprehensive network of 64 elementary reaction steps involving 7 gaseous molecules and 22 surface species is considered to account for the various possible reaction pathways during ESR over Ni (Table 2). The proposed network describes the molecular adsorption of the ethanol and water reactants (R1-4), with the absorbed water further dissociating towards hydroxyl (OH*) and oxygen (O*) surface species (R15-18). Absorbed ethanol dehydrogenation proceeds via two possible routes, leading to the formation of 1-hydroxyethyl (R19-20) and ethoxy (R21-22) species. Subsequent dehydrogenation steps of these intermediates (R23-26) lead to adsorbed acetaldehyde, the latter recognized to be a key intermediate in ESR [40]. Dehydrogenation of 1-hydroxyethyl can also proceed via 1-hydroxyethylidene to acetyl (R27-30), at which point three possible C-C cleavage steps are proposed: The C-C bond scission can occur directly after acetyl is formed to produce methyl species and carbon monoxide (R37-38) or after further dehydrogenation to CH_2CO* (R39-42) or CHCO* (R43-46). Acetaldehyde can similarly dehydrogenate to acetyl (R31-32) or decompose according to R33-36. Water-gas shift occurs via the reaction of carbon monoxide with either hydroxyl or oxygen surface species accounted for in reactions R47-52. Reactions R53-56 describe the (de)hydrogenation of CH_x* species, whilst methane steam reforming is accounted for in reactions R57-64. Carbon oxides and acetaldehyde are assumed to adsorb molecularly (R9-14) whereas methane and hydrogen adsorption proceeds dissociatively (R5-9).

3. Results

3.1. *Model validation*

The microkinetic model presented in the current work is fully parameterised on the basis of three sets of parameters: sticking coefficients, Arrhenius temperature exponents and chemisorption enthalpies (see Table 2 and Table 3). Initial values for chemisorption enthalpies were collected from experimental and DFT studies on Ni catalysts [30,41], while Arrhenius temperature exponents were initialised with values of 0. Sticking coefficients were kept equal at a value of 1 due to their low

impact on modelled outputs, while the coefficients γ used in equation (5) for the temperature dependence of chemisorption enthalpies were fixed at values obtained from previous studies [26,31]. Table 3 shows the final estimated values of the chemisorption enthalpies of species as well as γ coefficients, while the final values of the Arrhenius temperature exponents are reported in Table 2. The obtained values will be discussed in more detail in Section 3.5 pertaining to the evaluation of model parameters.

In order to evaluate the overall agreement between the model predicted and experimental results, parity plots for all gas molecules are presented in Figure 1. A satisfactory agreement over the entire experimental range for all detected molecules is visible. The parity plots for the reactants ethanol and water provide proof that the model is correctly describing the main activation pathways, while conversion pathways appear to be captured appropriately for all major products. Acetaldehyde shows the highest variance, most likely attributed to the lower order of magnitude of its molar flowrate values, as well as the comparatively higher difficulty of liquid products sampling and analysis. Nonetheless, acetaldehyde's detection is in line with the theoretical predictions of the Ni metal's affinity towards forming the species from ethanol [24] and the equivalent well established experimental observations of other groups on similar catalysts [40,42].

Performance curves are shown in Figure 2, presenting the effect of temperature, partial pressure of ethanol and water and space time on the conversion of ethanol and water as well as the carbon selectivities towards CO, CO_2, CH_4 and CH_3CHO. As indicated also from the parity plots, the model can reproduce to a good degree the experimental trends based on the reported parameter values in Table 2. As expected, the conversion of reactants increases with temperature (panel (a)). In line with our experimental observations [13], at low temperatures ethanol dehydrogenation leads to the production of acetaldehyde, while the carbon selectivity towards CO and CH_4 outweighs that of CO_2. As the temperature rises, the CO_2 selectivity increases and is accompanied by an equivalent decrease in the selectivities of CO, CH_4 and CH_3CHO, indicative of the promotion of secondary

reaction pathways. Results are specifically consistent with a rising contribution of the water gas shift reaction and the progressive promotion of the decomposition and oxidation of surface CH_x species, in equivalence to methane steam reforming mechanisms [43].

In order to elucidate the effect of reactants' partial pressures on the order of the reaction, two sets of experimental data obtained from the work of Zhurka et al. [13] were modelled. Results are presented in Figure 2 as H_2O/C variation, since these relate better to the observed selectivity trends, however the corresponding inlet partial pressures of the reactants are also indicated. Panel (b) shows the effect of ethanol partial pressure, maintaining the water partial pressure and total pressure constant, while panel (c) shows the inverse with water partial pressure varied and ethanol kept constant. Varying ethanol partial pressure, the model predicts that the conversion of ethanol and selectivity towards CO_2 are positively affected, while CH_4 and CO selectivities are negatively affected. The results on varying H_2O partial pressure show that ethanol conversion displays a mild decrease, however a positive influence is still observed for CO_2 selectivity accompanied by a negative effect for CH_4 and CO selectivity. For both partial pressure variation data sets, the above trends are well in line with the experimental observations of Zhurka et al. [13]. Selectivity trends are consistent with a promotion of secondary reactions by the increase of water derived surface species due to the rising H_2O/C ratio. Conversion profiles are better explained looking at Figure 3, where the model predicted and experimental partial reaction orders for ethanol and water are compared. A clearly positive order for ethanol (approximately equal to 0.5 as indicated by the square root of the partial pressure in the left panel) and a slightly negative order for water are visible, with the model reproducing the experimental trends very well, affirming that the kinetically relevant processes have been accurately captured. The positive order for ethanol is evidence of the participation of an ethanol-derived surface intermediate in the rate determining step, as stipulated in the analysis of the experimental work [13] and further elaborated with the microkinetic model in the following section. For the negative water reaction order, the partial coverages across this range of simulated conditions, shown in Table 4, reveal that the increase in the partial pressure of water leads to a

progressive catalyst surface saturation by adsorbed H_2O species, leading to a decreasing availability of active sites. Even though a rise in water-derived surface species, such as OH*, is indeed observed and explains the selectivity trends, overall a decrease in the coverage by adsorbed ethanol is predicted by the model that ultimately results in the observed decrease in conversion and supports the experimental findings. It is worth commenting that a similar negative order for water was observed in the experiments modelled by Sutton et al. [19], whereas the microkinetic model presented in that work predicted a zero order. That experimental negative order was attributed to support effects, namely excess water limiting ethanol activation on the Al_2O_3 support. In the present work, though, the SiO_2 support used was overall inert [13], hence the competitive adsorption of ethanol and water on the Ni metal is considered as the most probable reason for the experimental trends, which the model correctly describes.

With respect to the space time effect, the model is again able to predict sufficiently the experimental trends as is seen in panels (d) and (e) of Figure 2, but with some discrepancies in relation to acetaldehyde. Experimentally [13], results at low conversions (below 15-20%), indicated that temperature affects strongly the main reactive pathway of ethanol, the latter not involving acetaldehyde as an intermediate, at least at high temperatures. At 400^{o}C, acetaldehyde did appear as the sole primary product, as indicated also by its very high selectivity at the lowest space velocities studied, however at 550^{o}C CH_4 and CO also appeared as such. Qualitatively, the model predicts similar differences in the temperature dependence of the main reaction pathways, although milder to the experimentally observed and evident at relatively lower conversions (below 5%), as shown also from the suboptimal description of acetaldehyde's selectivity in panel (e) of Figure 2. Figure 4 shows the model predicted product selectivities as a function of ethanol conversion at different temperatures. At 400°C, as conversion approaches zero, acetaldehyde is indeed predicted to be the only product whose selectivity is increasing substantially, while at 550°C, CO, CH_4 and acetaldehyde selectivities are all clearly tending towards finite values at a zero conversion. More importantly, the model indeed predicts that the main pathway of ethanol conversion towards CH_4

and CO is not linked to adsorbed acetaldehyde and proceeds via another surface intermediate. The quantitative differences could potentially indicate that the assumptions made in relation to the mobility of the surface species during the development of the model are in need of revision or that the surface reaction energetics, as predicted by the semi-empirical UBI-QEP, require further refinement. Nonetheless, the overall very good agreement of the model-derived results with the experimental ones across a range of conditions, as highlighted in this section, allows using the model further in the following to obtain information on the kinetic importance of reaction steps.

3.2. *Kinetic relevance of reaction steps*

A sensitivity analysis of the model's parameters was carried out in order to investigate the kinetic relevance of the elementary surface reaction steps. A temperature of 400^{o}C and a $H_2O/C=3$ are selected to align with the conditions of the partial pressure variation runs. The pre-exponential factors of each reversible reaction pair were perturbed by a small fraction of their base value, the latter calculated by transition state theory as described in Section 2.2. The effect of this perturbation on the outlet molar fractions of reactants and products was quantified by the calculation of normalised sensitivity coefficients. Figure 5 shows the relevant results for ethanol. As discussed in the Introduction, previous studies [19,20,26] have identified the dehydrogenation pathways of ethanol as the kinetically relevant surface reactions, with the initial abstraction of H from the α-C, β-C or O of surface ethanol being in many cases the rate determining step. As seen in Figure 5, the most important steps identified in the current model via the sensitivity analysis are indeed along ethanol's dehydrogenation pathway and specifically are the secondary dehydrogenation of CH_3CHOH* to CH_3COH* and the further dehydrogenation of the latter to CH_3CO*, according to reactions R27-28 and R29-30, respectively. These findings are further in line with the experimental observations and the discussion in Section 3.1, as both of these steps are consistent with an overall reaction mechanism with a positive order in ethanol (Figure 3). Nonetheless, it bares notice and will be discussed further in the following section that these steps do not involve the ethoxy intermediate that is commonly accepted to be participating in the conversion of ethanol on Ni following an initial

O-H bond cleavage [17,24,44]. On the other hand, steam derived intermediates do not participate in these kinetically relevant steps and would suggest a zero order in water for the conversion of ethanol. As discussed previously though, the experimentally observed slightly negative order in water across a H_2O/C ratio that spans from sub-stoichiometric to large excess values is predicted by the model to be on account of surface saturation effects.

Figure 6 shows the results of the sensitivity analysis for the molar fractions of H_2O and products CO, CO_2, H_2, CH_4 and CH_3CHO. In line with the ethanol sensitivity analysis, R27-28 and R29-30 are the major kinetically relevant steps identified for all the gaseous products, having a positive effect to their production. A negative effect for the same reaction steps to the outlet molar fraction of H_2O is also identified and is consistent with the above results, as an increase in ethanol conversion and its decomposition products leads to a further consumption of water via secondary reactions. Nonetheless, reaction pair R59-60 is found to have the largest effect on H_2O, which, linked with the similar negative sensitivity for CH_4 and the positive one for CO, CO_2 and H_2, leads to the identification of these steps as the kinetically relevant ones for the methane steam reforming or CH_x oxidation sub-mechanism. For CH_3CHO, the effect of the same steps is the opposite to the gas products, meaning that the main ethanol consuming reactions lead to a decrease in the production of acetaldehyde. The latter fact, which will be discussed in more detail in the following, further suggests that the primary formation pathway of the acetaldehyde is not linked to the dominant conversion pathway of ethanol, as observed experimentally. This follows on the previous discussion of not identifying ethoxy as a key species, as the latter is the widely considered precursor to acetaldehyde [25]. In summary, the sensitivity analysis revealed R27-28 and R29-30 as the kinetically important steps under these conditions, a conclusion that will be elaborated in the next section, where the reaction steps involved in the overall reaction pathways are probed through a contribution analysis.

3.3. ***Reaction pathway analysis***

A differential contribution analysis at the outlet of the catalyst bed at the same conditions as the previous section is further carried out to clarify the significance of the various reaction pathways considered in the network. Specifically, the net production rates of all carbon containing species are considered in order to estimate their conversion percentages towards all other compounds. Results of this analysis are presented in Figure 7 and are further discussed below.

According to the model predictions, ethanol adsorbs on the catalyst surface via reaction R1, and then dehydrogenates via two main pathways. The dominant route proceeds via an α-dehydrogenation (R19) producing CH_3CHOH* with a high contribution of over 99% of the converted ethanol. Similar findings were reported in the work of Sutton et al. [19] which is one of the very few published works to have presented a comprehensive microkinetic model for ethanol steam reforming, although as commented earlier on a Pt metal catalyst. In the work of Koehle et al. [26], again a Pt catalyst was studied, but for ethanol partial oxidation, so understandably the high temperature oxidative conditions led to the surface pathways being substantially different to those discussed above, with ethanol activation proceeding primarily through dehydration. Similarly, the work of Baruah et al. [27], focusing on the oxidative steam reforming of ethanol on Rh, proposed dehydroxylation (C-O cleavage) as the initial ethanol activation step, although again for a different reaction and conditions. In the current work, in parallel to the main pathway to CH_3CHOH*, ethanol is predicted to also dehydrogenate successively first towards CH_3CH_2O* and then CH_3CHO* via reactions R21 and R25, which is well in line with the expected paths on Ni discussed previously [10,17,24,44]. Considering that these works, either experimental [17,44] or theoretical [10,24] referred to decomposition of ethanol on the close-packed Ni(111) surface, it cannot be excluded that the presence of low-coordinated sites and steam-derived O* and OH* species in our experiments promotes alternate dehydrogenation pathways [25].

Following the initial favoured α-dehydrogenation, the formed CH_3CHOH* continues dehydrogenating towards CH_3CHO* and CH_3COH* via R23 and R27, with the latter accounting for over 99% of conversion contribution, in line also with R27 having been identified as a key rate controlling step in Section 3.2. The formed CH_3COH* species further dehydrogenate exclusively towards CH_3CO* and CH_2CO* via reactions R29 and R39, the former of which was also identified as an important rate controlling step in Section 3.2. The model reports CH_2CO* as a key surface intermediate for the production of CO*, which aligns well with various works on the kinetics of ethanol steam reforming [11,19–21] all suggesting C-C bond scission to occur at CH_xCO* species of varying degrees of dehydrogenation. The current work predicts that the C-C bond cleavage takes place predominantly at the CH_2CO* intermediate leading to the formation of CH_2* and CO* via reaction R41.

CO* is predicted to follow two pathways, the less important of which contributes to surface CO* desorption and production of gas phase CO at an approximately 2% contribution. CO* follows primarily a water gas shift pathway, reacting with steam-derived OH* species to produce COOH* via reaction R48. CO* can, in principle, also react with O* to produce CO_2* directly via R52, however this pathway is not predicted to occur at the simulated conditions. COOH* is a primary species in the CO_2* production pathway, with the latter exclusively desorbing to the gas phase as CO_2. CH_2* species formed upon the C-C bond cleavage follow multiple pathways. The dominant one can be described as methane steam reforming with CH_2* reacting successively with 2 OH* species via reactions R57 and R59 to form COOH*, ultimately leading to gas phase CO_2. On the other hand, all CH_x* species, including CH_2*, can also hydrogenate up to CH_3*, the latter associatively desorbing as CH_4 via reaction R8. As such, the reaction pathway analysis further supports the discussion of previous sections and the experimental observations, suggesting the dominant ethanol conversion pathway on Ni to be that of decomposition, not involving dehydrogenation to acetaldehyde, the latter revealed to be a parallel and less important reaction path.

Concerning the non-carbon containing surface species, water, following its molecular adsorption, decomposes towards H* and OH*. The participation of OH* in various reactions and particularly R57, R59 and R48, accounts largely for the consumption of steam, whereas surface O* are predicted to participate to a much lesser extent. Surface hydrogen H* formed via multiple processes desorbs associatively for the production of gas phase hydrogen.

Based on the results of the space-velocity effect experiments, an additional case was considered to investigate the occurring changes in the reaction pathways at a low ethanol conversion of 3%. The pathways among species remain at these conditions overall similar, so the relevant plot is not shown, however the respective contributions of the initial ethanol conversion steps shift noticeably. The reactions producing acetaldehyde are comparatively promoted, with the dominant dehydrogenation pathway of adsorbed ethanol towards CH_3CHOH* now also contributing by a measureable 25.5% to the formation of CH_3CHO* via reaction R23 instead of only 0.15% seen in Figure 7. The secondary path to CH_3CH_2O*, leading exclusively to CH_3CHO* via reaction R25, also rises substantially in its contribution from 0.02% to as high as 17.6%. The above trends become more pronounced as conversion tends to zero values, and, given the lower adsorption enthalpy of CH_3CHO in comparison to CH_3 and CO (see Table 3), result in CH_3CHO appearing as a dominant product at low temperatures. At higher temperatures, the desorption of CH_4 and CO is enhanced leading to all three products appearing as primary ones.

3.4. ***Model parameter sensitivity***

A sensitivity analysis was also performed to discern the relevance of the model parameters of the microkinetic model, namely the adsorption enthalpies of considered species. Figure 8 shows results of the analysis in which normalised sensitivity coefficients were calculated for the outlet molar fractions of ethanol, CO, CO_2, CH_4, CH_3CHO and H_2 with a 1% perturbation of the model parameter values shown in Table 3. The adsorption enthalpy of CH_3CHOH is identified as having the highest positive effect on ethanol conversion, which, as expected, leads also to positively influencing the

production of CO, CO_2, CH_4 and H_2. UBI-QEP stipulates that an increase in the adsorption enthalpy of a compound will in turn lead to a higher or lower activation barrier for any reactions in which this compound participates as a reactant or product, respectively. Therefore, increasing the CH_3CHOH adsorption enthalpy causes the initial ethanol dehydrogenation to have a lower barrier, however it also increases the barrier of the follow-up dehydrogenations towards key intermediates CH_3CO* and CH_2CO*. At the same time, though, the stronger binding of CH_3CHOH to the surface enhances its partial coverage and, as such, the overall rate of reaction R27, leading to the simulated overall acceleration of the reaction pathway.

The second model parameter with an important positive effect on ethanol conversion is the chemisorption enthalpy of CH_3CO, which, as above, through partial coverage effects leads to a higher rate of production of key intermediate for C-C scission CH_2CO*, enhancing the dominant reaction pathway. The only other model parameter with a significant effect on the formation of products is the chemisorption enthalpy of OH, which, as also discussed in the previous section, is a co-reactant in most selectivity controlling reactions. The increased activation barrier for the reactions R48, R57, R59 should reduce the formation of key products, however OH* derives from water, which is the most abundant reactant. A higher OH chemisorption enthalpy, therefore, has a positive effect on H_2O* dissociation, which in turn leads to a rise in the partial coverage of OH*, thus leading to a much faster reaction rate for the production of gas phase products CO and CO_2. For example, at 400°C and H_2O/C of 3 with an inlet water partial pressure of 0.37 bar, the partial coverages of H_2O* and OH* are predicted to be 0.52 and 0.002 respectively, with an OH chemisorption enthalpy of 242 kJ mol^{-1}. An increase of the OH chemisorption enthalpy to 245 kJ mol^{-1} at the same conditions changes the coverages of H_2O* and OH* to 0.516 and 0.037, respectively, hence a substantially higher hydroxyl coverage is achieved. CH_4 formation as expected is negatively affected by the stronger binding of OH, as CH_2*, the main precursor to its production, is a reactant in the methane steam reforming pathway.

The sensitivity analysis also identifies strong negative influences on the conversion of ethanol from the chemisorption enthalpies of CH_3, H and H_2O. As the C-C bond cleavage in reaction R41 leads to an even production of CH_2* and CO* it follows that at the point of scission these products are equally abundant on the surface. Therefore, whilst CO* further participates in the water-gas shift sub-mechanism, an increase in the adsorption enthalpy of CH_3 leads to the methane steam reforming pathway becoming less prominent, thus explaining the negative effect on the production of CO and CO_2. The increase in the CH_3 binding strength also causes the desorption rate of methane to be reduced explaining the negative effect on CH_4 production. The drop in the conversion of ethanol is propagated by the gradual saturation of the catalyst active sites by surface CH_3*, with this saturation leading to a reduced rate of reaction in the main ethanol dehydrogenation pathway. H* is a product of all dehydrogenation reactions and, therefore, an increase in its adsorption enthalpy leads to the surface being saturated easily by this species, explaining again the negative effect of the parameter on conversion and product formation. Similarly, and as discussed in relation to the partial pressure variation experiments, a stronger H_2O binding leads to a progressively more saturated surface.

3.5. *Estimated model parameters evaluation*

Table 3 shows the final estimated values, following regression, for the adsorption enthalpies of the microkinetic model, while the temperature exponent values can be seen in Table 2. As described in Section 2.1, the initial values for chemisorption enthalpies of all species during model development were obtained from literature DFT and prior experimental studies. After model parameter sensitivity analysis was conducted (Figure 8), parameters with little or no sensitivity were fixed at the literature obtained values in order to allow for higher confidence in the regression of the more sensitive ones. Estimated parameters shown in Table 3 have narrow confidence intervals evidencing a low standard error. The maximum value for the correlation coefficient between two parameters occurs between Q_{H_2O} and Q_{CH_3CHOH} and has a value of -0.86 most likely related to the negative relationship between the surface coverages of both species, as discussed in the previous section. The squared multiple

correlation coefficient value obtained for the regression was sufficiently close to unity (R^2=0.886), which, coupled with the high F-value of 215.61 (tabulated value = 3.01) for the significance of the regression, affirms the model's good performance.

All chemisorption enthalpies estimated conform to physically realistic values and show adequate agreement with theoretical and experimentally reported ones. The presently estimated value for CH_3, 200.48 kJ mol^{-1}, is only slightly higher than various reported values. In particular, a DFT study for the steam reforming of acetic acid on the Ni (111) [41] surface reports a CH_3 chemisorption enthalpy value of 191.97 kJ mol^{-1}. With respect to H, a very good agreement for the estimated value of 257 kJ mol^{-1} in this work can be seen in literature with different reported values usually ranging from 240 to 270 kJ mol^{-1} [30,41,45]. Similarly, the estimated values of OH and H_2O (242.2 kJ mol^{-1} and 58.95 kJ mol^{-1} respectively) both fall within the range of reported DFT or experimental values (see references above). The weak binding of HCHO on Ni (111) as reported by Remediakis et al. [45] is qualitatively well reproduced with an estimated adsorption enthalpy in this work of 23.68 kJ mol^{-1}. For ethanol decomposition derived surface species, the estimated values of chemisorption enthalpies presented in Table 3 all lie within the range of observed literature published values [11,41,45,46]. Values of 191.39 kJ mol^{-1} and 83.61 kJ mol^{-1} were estimated for CH_3CO and CH_2CO, respectively, comparing very well with the equivalent 202.62 kJ mol^{-1} and 83.94 kJ mol^{-1} reported by Ran et al. [41]. In summary, the parameterisation of the model based on the above adsorption enthalpies was demonstrated to describe successfully the experimental data and provided insight on the mechanistic trends of the ethanol steam reforming process over Ni catalysts when support effects are not dominant.

4. Conclusions

In the current work a microkinetic model is presented for ethanol steam reforming over a Ni/SiO_2 catalyst, the later metal selected on account of its favourable economics in comparison to noble metals. The model is used to simulate an experimental data set that spans a wide range of

conditions. All kinetic parameters are either a priori determined or correlated with the adsorption enthalpies of participating species. This allows carrying out a sensitivity analysis that reveals the relative importance of adsorption enthalpies in the kinetic mechanism. Experimental observations relating to a positive reaction order for ethanol were able to be linked to its kinetically determining dehydrogenation to 1-hydroxyethyl, while the negative order for steam was shown to be due to a progressive saturation of the surface of the catalyst by water. The consideration of secondary surface reactions of ethanol decomposition products, describing methane steam reforming and water gas shift, was revealed necessary for the explanation of the experimentally observed selectivities across the broad range of conditions simulated. The predicted decomposition pathways share similarities to previously reported by other microkinetic studies on noble metals, however differences with DFT calculations on Ni(111) are identified and suggest that under reforming conditions and over "real" catalysts different surface steps might be preferred. This model's results serve as a basis for and prompt the development of consolidated kinetic schemes that incorporate the effect of supports on the ethanol steam reforming mechanism.

Acknowledgements

Funding for this work was provided by the University of Aberdeen and Curtin University under the 'Aberdeen-Curtin Alliance'.

References

[1] N. Sanchez, R.Y. Ruiz, B. Cifuentes, M. Cobo, Hydrogen from glucose: A combined study of glucose fermentation, bioethanol purification, and catalytic steam reforming, Int. J. Hydrogen Energy. 41 (2016) 5640–5651.

[2] H. Song, L. Zhang, R.B. Watson, D. Braden, U.S. Ozkan, Investigation of bio-ethanol steam reforming over cobalt-based catalysts, Catal. Today. 129 (2007) 346–354.

[3] M. Ni, D.Y.C. Leung, M.K.H. Leung, A review on reforming bio-ethanol for hydrogen production, Int. J. Hydrogen Energy. 32 (2007) 3238–3247.

[4] C. Rioche, S. Kulkarni, M. Meunier, J. Breen, R. Burch, Steam reforming of model compounds and fast pyrolysis bio-oil on supported noble metal catalysts, Appl. Catal. B Environ. 61 (2005) 130–139.

[5] R. González-Gil, I. Chamorro-Burgos, C. Herrera, M.A. Larrubia, M. Laborde, F. Mariño, L.J. Alemany, Production of hydrogen by catalytic steam reforming of oxygenated model compounds on Ni-modified supported catalysts. Simulation and experimental study, Int. J. Hydrogen Energy. 40 (2015) 11217–11227.

[6] R. Trane, S. Dahl, M.S. Skjøth-Rasmussen, A.D. Jensen, Catalytic steam reforming of bio-oil, Int. J. Hydrogen Energy. 37 (2012) 6447–6472.

[7] P.D. Vaidya, A.E. Rodrigues, Insight into steam reforming of ethanol to produce hydrogen for fuel cells, Chem. Eng. J. 117 (2006) 39–49.

[8] L. V Mattos, G. Jacobs, B.H. Davis, F.B. Noronha, Production of hydrogen from ethanol: Review of reaction mechanism and catalyst deactivation, Chem. Rev. 112 (2012) 4094–4123.

[9] F. Wang, W. Cai, C. Descorme, H. Provendier, W. Shen, C. Mirodatos, Y. Schuurman, From mechanistic to kinetic analyses of ethanol steam reforming over Ir/CeO_2 catalyst, Int. J. Hydrogen Energy. 39 (2014) 18005–18015.

[10] J.H. Wang, C.S. Lee, M.C. Lin, Mechanism of ethanol reforming: Theoretical foundations, J. Phys. Chem. C. 113 (2009) 6681–6688.

[11] I. Llera, V. Mas, M.L. Bergamini, M. Laborde, N. Amadeo, Bio-ethanol steam reforming on Ni based catalyst. Kinetic study, Chem. Eng. Sci. 71 (2012) 356–366.

[12] A. Akande, A. Aboudheir, R. Idem, A. Dalai, Kinetic modeling of hydrogen production by the catalytic reforming of crude ethanol over a co-precipitated Ni - Al_2O_3 catalyst in a packed bed tubular reactor, Int. J. Hydrogen Energy. 31 (2006) 1707–1715.

[13] M.D. Zhurka, A.A. Lemonidou, J.A. Anderson, P.N. Kechagiopoulos, Kinetic analysis of the steam reforming of ethanol over Ni/SiO_2 for the elucidation of metal-dominated reaction pathways, React. Chem. Eng. 3 (2018) 883–897.

[14] R. Alcalá, M. Mavrikakis, J.A. Dumesic, DFT studies for cleavage of C-C and C-O bonds in surface species derived from ethanol on Pt(111), J. Catal. 218 (2003) 178–190.

[15] F. Soyal-Baltacioğlu, A.E. Aksoylu, Z.I. Önsan, Steam reforming of ethanol over Pt-Ni Catalysts, Catal. Today. 138 (2008) 183–186.

[16] M. Li, W. Guo, R. Jiangs, L. Zhao, H. Shan, Decomposition of ethanol on Pd(111): A density functional theory stutdy, Langmuir. 26 (2010) 1879–1888.

[17] S.M. Gates, J.N. Russell, J.T. Yates, Bond activation sequence observed in the chemisorption and surface reaction of ethanol on Ni(111), Surf. Sci. 171 (1986) 111–134.

[18] P. Ferrin, D. Simonetti, S. Kandoi, E. Kunkes, J.A. Dumesic, J.K. Nørskov, M. Mavrikakis, Modeling ethanol decomposition on transition metals: A combined application of scaling and brønsted-evans-polanyi relations, J. Am. Chem. Soc. 131 (2009) 5809–5815.

[19] J.E. Sutton, P. Panagiotopoulou, X.E. Verykios, D.G. Vlachos, Combined DFT, microkinetic, and experimental study of ethanol steam reforming on Pt, J. Phys. Chem. C. 117 (2013) 4691–4706.

[20] M. Li, W. Guo, R. Jiang, L. Zhao, X. Lu, H. Zhu, D. Fu, H. Shan, Density functional study of ethanol decomposition on Rh(111), J. Phys. Chem. C. 114 (2010) 21493–21503.

[21] J. Zhang, Z. Zhong, X.-M. Cao, P. Hu, M.B. Sullivan, L. Chen, Ethanol steam reforming on Rh

catalysts: Theoretical and experimental understanding, ACS Catal. 4 (2014) 448–456.

[22] Y. Ma, L. Hernández, C. Guadarrama-Pérez, P.B. Balbuena, Ethanol reforming on Co(0001) surfaces: A density functional theory study, J. Phys. Chem. A. 116 (2012) 1409–1416.

[23] D.R. Sahoo, S. Vajpai, S. Patel, K.K. Pant, Kinetic modeling of steam reforming of ethanol for the production of hydrogen over Co/Al_2O_3 catalyst, Chem. Eng. J. 125 (2007) 139–147.

[24] J.E. Sutton, D.G. Vlachos, Ethanol Activation on Closed-Packed Surfaces, Ind. Eng. Chem. Res. 54 (2015) 4213–4225.

[25] D. Zanchet, J.B.O. Santos, S. Damyanova, J.M.R. Gallo, J.M.C. Bueno, Toward understanding metal-catalyzed ethanol reforming, ACS Catal. 5 (2015) 3841–3863.

[26] M. Koehle, A. Mhadeshwar, Microkinetic modeling and analysis of ethanol partial oxidation and reforming reaction pathways on platinum at short contact times, Chem. Eng. Sci. 78 (2012) 209–225.

[27] R. Baruah, M. Dixit, A. Parejiya, P. Basarkar, A. Bhargav, S. Sharma, Oxidative steam reforming of ethanol on rhodium catalyst – I: Spatially resolved steady-state experiments and microkinetic modeling, Int. J. Hydrogen Energy. 42 (2017) 10184–10198.

[28] K. Metaxas, J. Thybaut, G. Morra, D. Farrusseng, C. Mirodatos, G. Marin, A microkinetic vision on high-throughput catalyst formulation and optimization: Development of an appropriate software tool, Top. Catal. 53 (2010) 64–76.

[29] C. Sprung, P.N. Kechagiopoulos, J.W. Thybaut, B. Arstad, U. Olsbye, G.B. Marin, Microkinetic evaluation of normal and inverse kinetic isotope effects during methane steam reforming to synthesis gas over a $Ni/NiAl_2O_4$ model catalyst, Appl. Catal. A Gen. 492 (2015) 231–242.

[30] P.N. Kechagiopoulos, S.D. Angeli, A.A. Lemonidou, Low temperature steam reforming of methane: A combined isotopic and microkinetic study, Appl. Catal. B Environ. 205 (2017) 238–253.

[31] A.B. Mhadeshwar, H. Wang, D.G. Vlachos, Thermodynamic Consistency in Microkinetic Development of Surface Reaction Mechanisms, J. Phys. Chem. B. 107 (2003) 12721–12733.

[32] J.A. Dumesic, D.F. Rudd, L.M. Aparicio, J.E. Rekoske, A.A. Treviño, The Microkinetics of heterogeneous catalysis, American Chemical Society, 1993.

[33] M. Faheem, M. Saleheen, J. Lu, A. Heyden, Ethylene glycol reforming on Pt(111): First-principles microkinetic modeling in vapor and aqueous phases, Catal. Sci. Technol. 6 (2016) 8242–8256.

[34] E. Shustorovich, The Bond-Order Conservation Approach to Chemisorption and Heterogeneous Catalysis: Applications and Implications, Adv. Catal. 37 (1990) 101–163.

[35] E. Shustorovich, H. Sellers, The UBI-QEP method: A practical theoretical approach to understanding chemistry on transition metal surfaces, Surf. Sci. Rep. 31 (1998) 1–119.

[36] P.N. Brown, A.C. Hindmarsh, L.R. Petzold, Using Krylov methods in the solution of large-scale differential-algebraic systems, SIAM J. Sci. Comput. 15 (1994) 1467–1488.

[37] H.H. Rosenbrock, An Automatic Method for Finding the Greatest or Least Value of a Function, Comput. J. 3 (1960) 175–184.

[38] D.W. Marquardt, An algorithm for least-squares estimation of nonlinear parameters, J. Soc. Ind. Appl. Math. 11 (1963) 431–441.

[39] P.T. Boggs, J.R. Donaldson, R. h. Byrd, R.B. Schnabel, Algorithm 676: ODRPACK: software for weighted orthogonal distance regression, ACM Trans. Math. Softw. 15 (1989) 348–364.

[40] A.N. Fatsikostas, X.E. Verykios, Reaction network of steam reforming of ethanol over Ni-based catalysts, J. Catal. 225 (2004) 439–452.

[41] Y.X. Ran, Z.Y. Du, Y.P. Guo, J. Feng, W.Y. Li, Density functional theory study of acetic acid steam reforming on Ni(111), Appl. Surf. Sci. 400 (2017) 97–109.

[42] J. Vicente, J. Ereña, C. Montero, M.J. Azkoiti, J. Bilbao, A.G. Gayubo, Reaction pathway for ethanol steam reforming on a Ni/SiO_2 catalyst including coke formation, Int. J. Hydrogen Energy. 39 (2014) 18820–18834.

[43] J.W.C. Liberatori, R.U. Ribeiro, D. Zanchet, F.B. Noronha, J.M.C. Bueno, Steam reforming of ethanol on supported nickel catalysts, Appl. Catal. A Gen. 327 (2007) 197–204.

[44] J. Xu, X. Zhang, R. Zenobi, J. Yoshinobu, Z. Xu, J.T. Yates, Ethanol decomposition on Ni(111): observation of ethoxy formation by IRAS and other methods, Surf. Sci. 256 (1991) 288–300.

[45] I.N. Remediakis, F. Abild-Pedersen, J.K. Nørskov, DFT study of formaldehyde and methanol synthesis from CO and H_2 on Ni(111), J. Phys. Chem. B. 108 (2004) 14535–14540.

[46] O. Skoplyak, M.A. Barteau, J.G. Chen, Ethanol and ethylene glycol on Ni/Pt(1 1 1) bimetallic surfaces: A DFT and HREELS study, Surf. Sci. 602 (2008) 3578–3587.

[47] W. Zhao, S.J. Carey, S.E. Morgan, C.T. Campbell, Energetics of adsorbed formate and formic acid on Ni(111) by calorimetry, J. Catal. 352 (2017) 300–304.

Table 1. Experimental operating conditions and catalyst properties.

Catalyst	Ni/SiO_2
Ni loading (wt %)	10
Ni dispersion (%)	38.6
Surface area ($m^2\ g^{-1}$)	105.32
Catalyst weight per experiment (g)	0.08
Temperature (°C)	300 – 550
H_2O/C (mol mol^{-1})	1 – 6
Partial pressure of ethanol (bar)	0.03 – 0.18
Partial pressure of water (bar)	0.12 – 0.74
$W/F_{Eth,t0}$ (g_{cat} s g_{Eth}^{-1})	58.2 – 349.4

Table 2. Microkinetic model for ethanol steam reforming on Ni/SiO_2. Activation barriers are calculated using the model parameters shown in Table 3 via UBI-QEP and pre-exponential factors calculated via transition state theory as described in Section 2.2. Modified Arrhenius equation used of form $R_i^f = A_i \cdot T^{\beta} \cdot e^{-E_a/RT}$ with the temperature exponents reported below.

No.	Reaction	E_a (kJ mol^{-1})	A (s^{-1})	Temperature exponent, β
R1	$CH_3CH_2OH + * \rightarrow CH_3CH_2OH*$	0.00	$3.33 \times 10^{+04}$	0.0
R2	$CH_3CH_2OH* \rightarrow CH_3CH_2OH + *$	43.49	$3.51 \times 10^{+13}$	0.0
R3	$H_2O + * \rightarrow H_2O*$	0.00	$5.32 \times 10^{+04}$	0.0
R4	$H_2O* \rightarrow H_2O + *$	53.07	$1.37 \times 10^{+13}$	0.0
R5	$H_2 + 2* \rightarrow H* + H*$	30.92	$1.59 \times 10^{+05}$	0.0
R6	$H* + H* \rightarrow H_2 + 2*$	97.58	$4.19 \times 10^{+12}$	0.0
R7	$CH_4 + 2* \rightarrow CH_3* + H*$	55.53	$5.64 \times 10^{+04}$	0.0
R8	$CH_3* + H* \rightarrow CH_4 + 2*$	57.10	$2.26 \times 10^{+12}$	-2.0±0.035
R9	$CO + * \rightarrow CO*$	0.00	$4.27 \times 10^{+04}$	0.0
R10	$CO* \rightarrow CO + *$	98.74	$2.14 \times 10^{+13}$	1.5±0.0436
R11	$CO_2 + * \rightarrow CO_2*$	0.00	$3.40 \times 10^{+04}$	0.0
R12	$CO_2* \rightarrow CO_2 + *$	20.97	$3.36 \times 10^{+13}$	0.0
R13	$CH_3CHO + * \rightarrow CH_3CHO*$	0.00	$3.40 \times 10^{+04}$	0.0
R14	$CH_3CHO* \rightarrow CH_3CHO + *$	74.52	$3.36 \times 10^{+13}$	2.0±0.0091
R15	$H_2O* + * \rightarrow OH* + H*$	93.59	$1.44 \times 10^{+13}$	0.0
R16	$OH* + H* \rightarrow H_2O* + *$	29.02	$2.00 \times 10^{+13}$	0.0
R17	$OH* + * \rightarrow O* + H*$	63.92	$3.19 \times 10^{+13}$	0.0
R18	$O* + H* \rightarrow OH* + *$	98.61	$4.90 \times 10^{+13}$	0.0
R19	$CH_3CH_2OH* + * \rightarrow CH_3CHOH* + H*$	58.92	$7.83 \times 10^{+12}$	0.0
R20	$CH_3CHOH* + H* \rightarrow CH_3CH_2OH* + *$	42.61	$1.51 \times 10^{+13}$	0.0
R21	$CH_3CH_2OH* + * \rightarrow CH_3CH_2O* + H*$	74.72	$1.00 \times 10^{+12}$	0.0
R22	$CH_3CH_2O* + H* \rightarrow CH_3CH_2OH* + *$	36.81	$1.93 \times 10^{+13}$	0.0
R23	$CH_3CHOH* + * \rightarrow CH_3CHO* + H*$	53.73	$1.91 \times 10^{+11}$	0.0
R24	$CH_3CHO* + H* \rightarrow CH_3CHOH* + *$	3.86	$1.42 \times 10^{+13}$	0.0
R25	$CH_3CH_2O* + * \rightarrow CH_3CHO* + H*$	45.63	$1.91 \times 10^{+11}$	0.0
R26	$CH_3CHO* + H* \rightarrow CH_3CH_2O* + *$	17.28	$1.42 \times 10^{+13}$	0.0
R27	$CH_3CHOH* + * \rightarrow CH_3COH* + H*$	46.07	$1.91 \times 10^{+11}$	0.0
R28	$CH_3COH* + H* \rightarrow CH_3CHOH* + *$	29.65	$1.42 \times 10^{+13}$	0.0
R29	$CH_3COH* + * \rightarrow CH_3CO* + H*$	20.14	$1.51 \times 10^{+13}$	0.0
R30	$CH_3CO* + H* \rightarrow CH_3COH* + *$	87.78	$5.64 \times 10^{+11}$	0.0
R31	$CH_3CHO* + * \rightarrow CH_3CO* + H*$	3.41	$1.10 \times 10^{+12}$	0.0
R32	$CH_3CO* + H* \rightarrow CH_3CHO* + *$	104.50	$3.38 \times 10^{+13}$	0.0
R33	$CH_3CHO* + * \rightarrow CH_3* + CHO*$	11.82	$1.00 \times 10^{+11}$	0.0
R34	$CH_3* + CHO* \rightarrow CH_3CHO* + *$	87.01	$2.10 \times 10^{+09}$	0.0
R35	$CHO* + * \rightarrow CO* + H*$	0.00	$6.60 \times 10^{+11}$	0.0
R36	$CO* + H* \rightarrow CHO* + *$	81.97	$1.67 \times 10^{+13}$	0.0
R37	$CH_3CO* + * \rightarrow CH_3* + CO*$	4.71	$2.08 \times 10^{+12}$	0.0
R38	$CH_3* + CO* \rightarrow CH_3CO* + *$	60.79	$1.34 \times 10^{+13}$	0.0
R39	$CH_3CO* + * \rightarrow CH_2CO* + H*$	50.90	$4.24 \times 10^{+12}$	0.0
R40	$CH_2CO* + H* \rightarrow CH_3CO* + *$	9.47	$1.66 \times 10^{+13}$	0.0
R41	$CH_2CO* + * \rightarrow CH_2* + CO*$	2.07	$7.43 \times 10^{+11}$	0.0
R42	$CH_2* + CO* \rightarrow CH_2CO* + *$	76.55	$1.93 \times 10^{+12}$	0.0
R43	$CH_2CO* + * \rightarrow CHCO* + H*$	81.57	$1.15 \times 10^{+13}$	0.0
R44	$CHCO* + H* \rightarrow CH_2CO* + *$	40.29	$1.65 \times 10^{+13}$	0.0

R45	$CHCO^* + * \rightarrow CH^* + CO^*$	0.00	$5.18 \times 10^{+11}$	0.0
R46	$CH^* + CO^* \rightarrow CHCO^* + *$	107.61	$3.74 \times 10^{+12}$	0.0
R47	$COOH^* + * \rightarrow CO^* + OH^*$	44.88	$7.56 \times 10^{+10}$	0.0
R48	$CO^* + {}^*OH \rightarrow COOH^* + *$	24.87	$1.10 \times 10^{+12}$	0.0
R49	$COOH^* + * \rightarrow CO_2^* + H^*$	0.79	$1.42 \times 10^{+11}$	0.0
R50	$CO_2^* + H^* \rightarrow COOH^* + *$	18.58	$1.54 \times 10^{+13}$	0.0
R51	$CO_2^* + * \rightarrow CO^* + O^*$	40.24	$1.93 \times 10^{+12}$	0.0
R52	$CO^* + O^* \rightarrow CO_2^* + *$	55.93	$1.15 \times 10^{+13}$	0.0
R53	$CH_3^* + * \rightarrow CH_2^* + H^*$	88.00	$1.03 \times 10^{+13}$	0.0
R54	$CH_2^* + H^* \rightarrow CH_3^* + *$	64.97	$7.38 \times 10^{+12}$	0.0
R55	$CH_2^* + * \rightarrow CH^* + H^*$	90.89	$8.03 \times 10^{+12}$	0.0
R56	$CH^* + H^* \rightarrow CH_2^* + *$	82.75	$3.19 \times 10^{+13}$	0.0
R57	$CH_2^* + OH^* \rightarrow HCHO^* + H^*$	22.27	$2.35 \times 10^{+10}$	0.0
R58	$HCHO^* + H^* \rightarrow CH_2^* + OH^*$	7.80	$3.77 \times 10^{+11}$	0.0
R59	$HCHO^* + OH^* \rightarrow HCOOH^* + H^*$	0.00	$2.89 \times 10^{+12}$	0.0
R60	$HCOOH^* + H^* \rightarrow HCHO^* + OH^*$	94.28	$9.75 \times 10^{+12}$	0.0
R61	$HCOOH^* + * \rightarrow COOH^* + H^*$	36.01	$1.70 \times 10^{+13}$	0.0
R62	$COOH^* + H^* \rightarrow HCOOH^* + *$	88.65	$3.10 \times 10^{+12}$	0.0
R63	$CH_2^* + {}^*O \rightarrow CHO^* + H^*$	58.14	$1.42 \times 10^{+13}$	0.0
R64	$CHO^* + H^* \rightarrow CH_2^* + O^*$	53.91	$1.51 \times 10^{+13}$	0.0

Table 3. Estimated model parameters with 95% confidence intervals. Chemisorption enthalpy values without confidence intervals were adopted from the literature sources shown, while those with confidence intervals were regressed using as initial values the respective literature sources shown.

Species	Chemisorption enthalpy, Q (kJ mol^{-1})	Sources for initial or used value	Temperature dependence coefficient $\boldsymbol{\gamma}$ in equation (5) [31]
CH_3CH_2OH	45.84	[46]	2.5
H_2O	58.95±0. 69	[41]	2.5
CO_2	25.68	[30,41]	2.0
CH_3CH_2O	171.54	[46]	2.5
CH_3CHO	71.04	[41]	2.5
OH	242.2±0. 87	[41,45]	2.0
H	257.0±0. 66	[41,47]	1.5
CH_3	200.48±0. 59	[30,41]	2.5
CH_2	391.73	[30]	2.5
CH	556.07	[30]	2.0
CO	113.44	[30]	2.0
CHO	206.69	[30]	2.5
HCHO	23.68±0.38	[45]	2.5
HCOOH	65.01	[47]	2.5
CH_3CO	191.39±0.91	[41]	2.0
CH_2CO	83.61±0.18	[41]	2.0
CHCO	283.94	[41]	2.0
COOH	250.01	[30]	2.0
O	453.0	[30]	1.0
CH_3CHOH	180±2.21	[46]	2.5
CH_3COH	213.8	[41]	2.5

Table 4. Effect of partial pressure of water on partial coverage of surface species at 400°C.

Partial pressure (bar)		Partial coverage of catalyst surface (-)				
C_2H_5OH	H_2O	C_2H_5OH*	H_2O*	H*	OH*	Vacant site
0.06	0.12	8.86×10^{-3}	0.41	8.94×10^{-2}	1.49×10^{-3}	0.31
0.06	0.25	5.35×10^{-3}	0.50	5.92×10^{-2}	1.89×10^{-3}	0.21
0.06	0.37	3.87×10^{-3}	0.52	4.69×10^{-2}	2.06×10^{-3}	0.18
0.06	0.49	2.94×10^{-3}	0.53	3.86×10^{-2}	2.18×10^{-3}	0.15
0.06	0.61	2.45×10^{-3}	0.55	3.24×10^{-2}	2.27×10^{-3}	0.13
0.06	0.74	2.10×10^{-3}	0.57	2.75×10^{-2}	2.33×10^{-3}	0.11

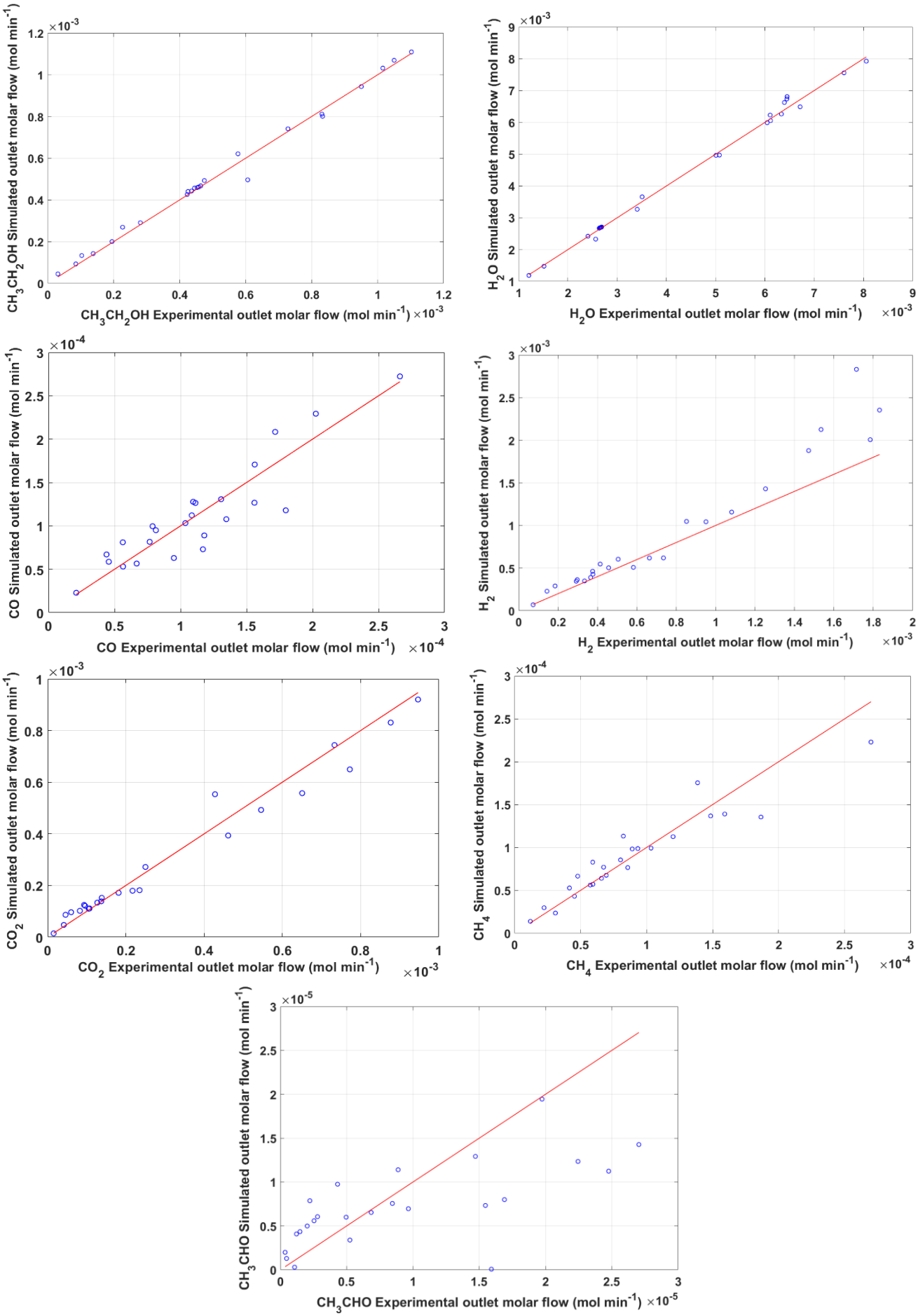

Figure 1. Parity diagrams for detected liquid and gas components at conditions reported in Table 1 and discussed in Zhurka et al. [13]. Modelling results have been obtained with the parameter values shown in Table 3.

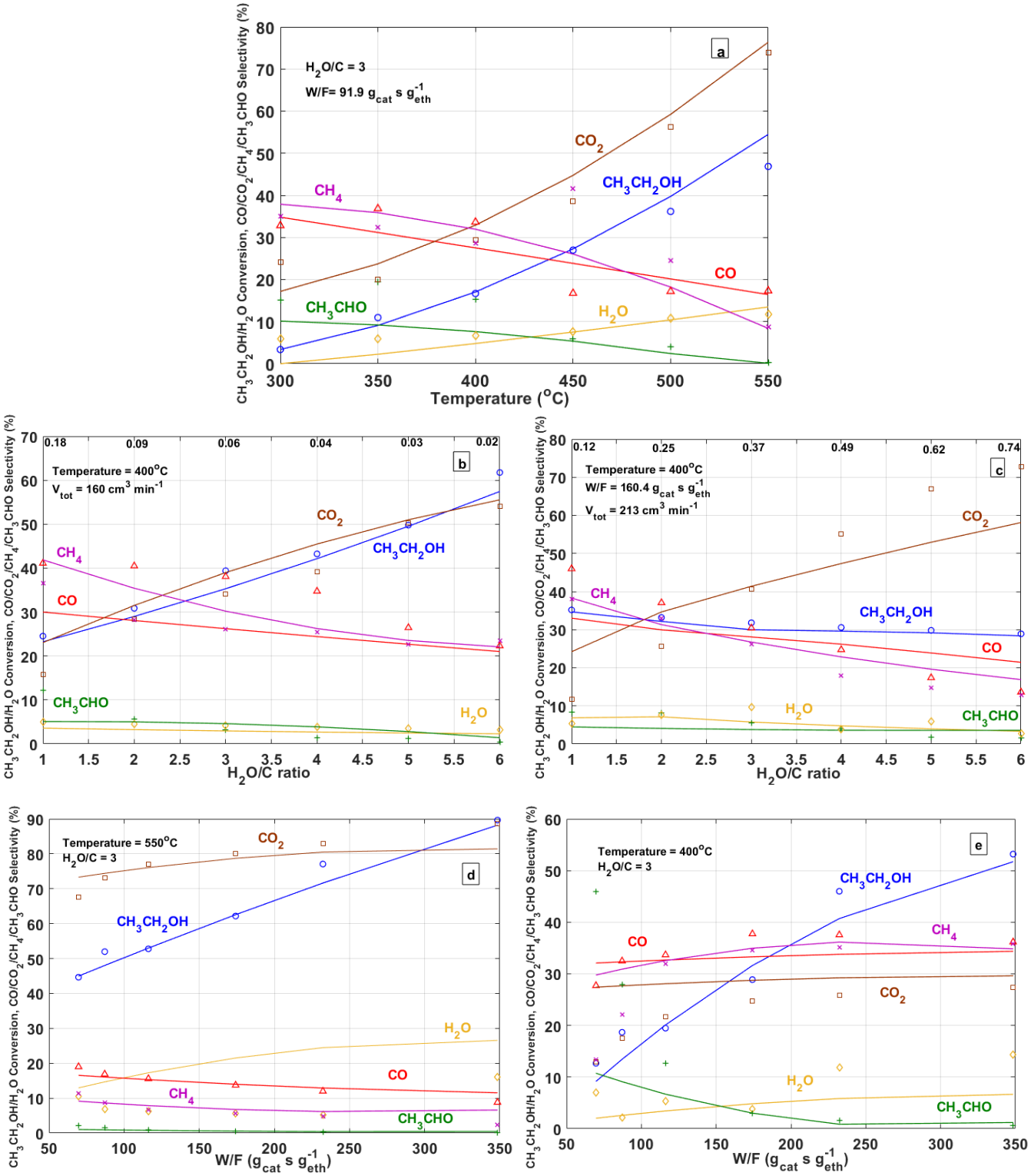

Figure 2. Comparison of model predicted conversions and selectivities over Ni/SiO_2 catalyst (lines) with experimental results (symbols). Operating conditions are indicated on the respective panels.

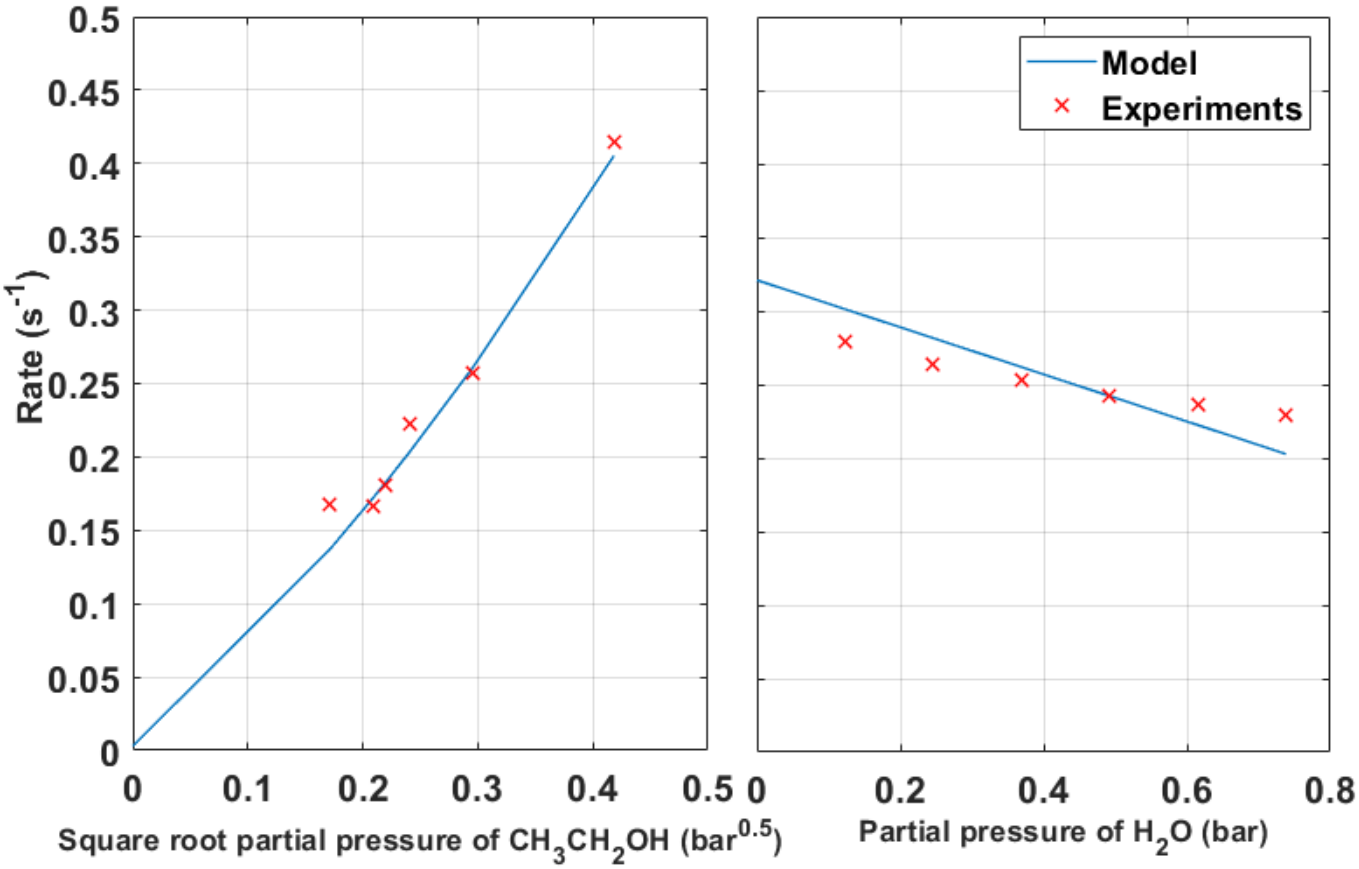

Figure 3. Reaction orders with respect to ethanol and water partial pressure (operating conditions are that of Figure 2 panels b and c respectively).

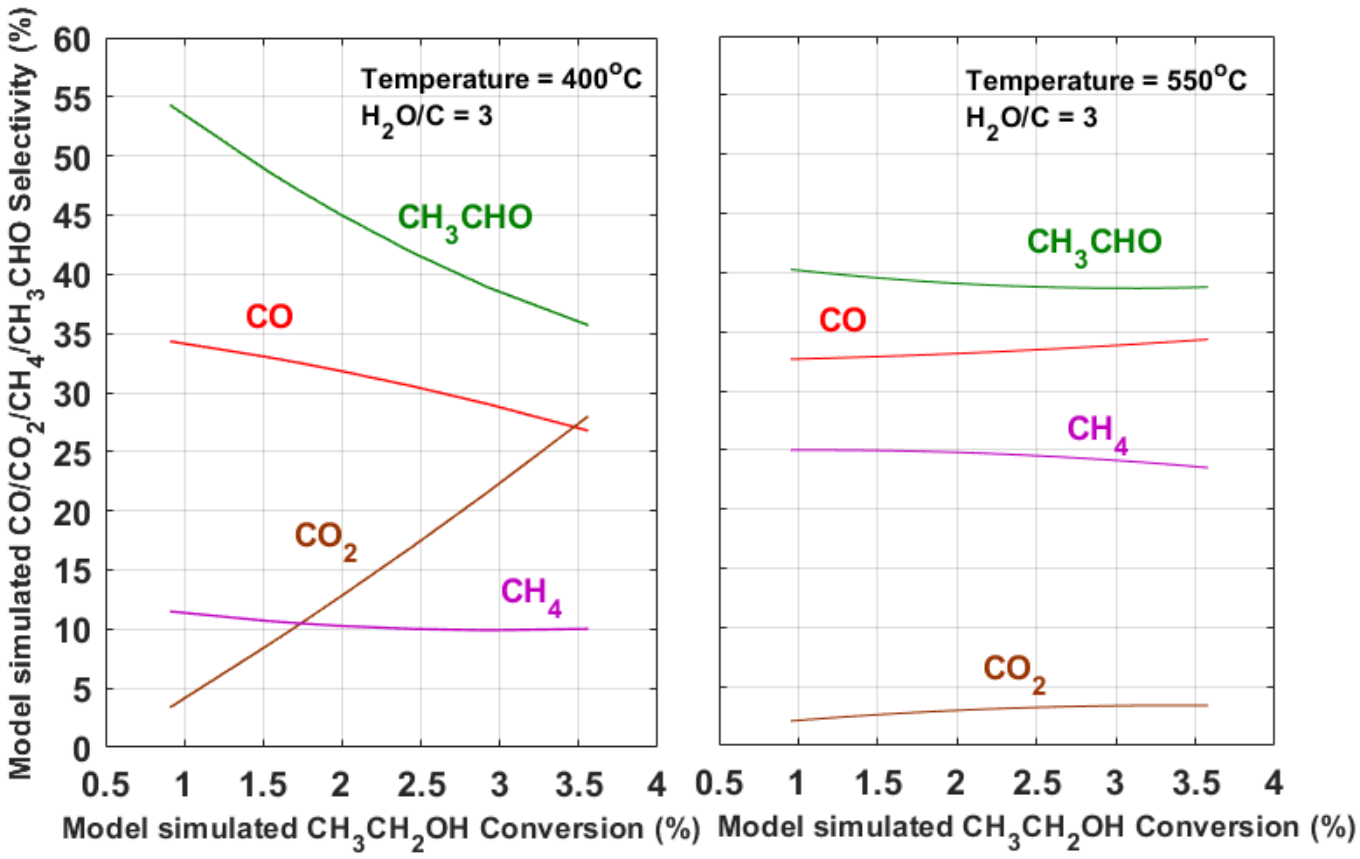

Figure 4. Ethanol conversion versus products selectivities depicting primary and secondary products at different temperatures (Operating conditions are shown in the respective panels).

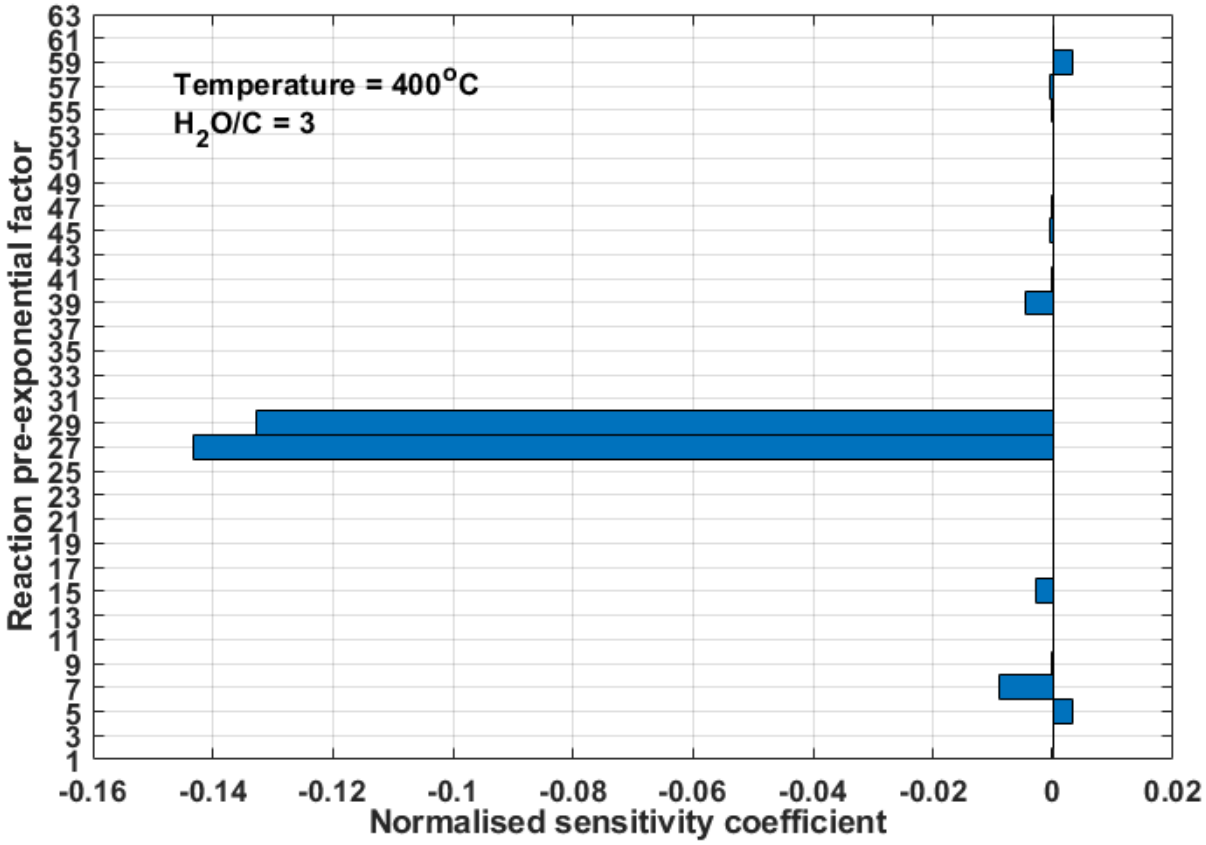

Figure 5. Sensitivity analysis of pre-exponential factors of microkinetic model reactions shown in Table 2, at 400°C and $H_2O/C=3$ for ethanol outlet molar fraction. Base values for pre-exponential factors are calculated as described in Section 2.2.

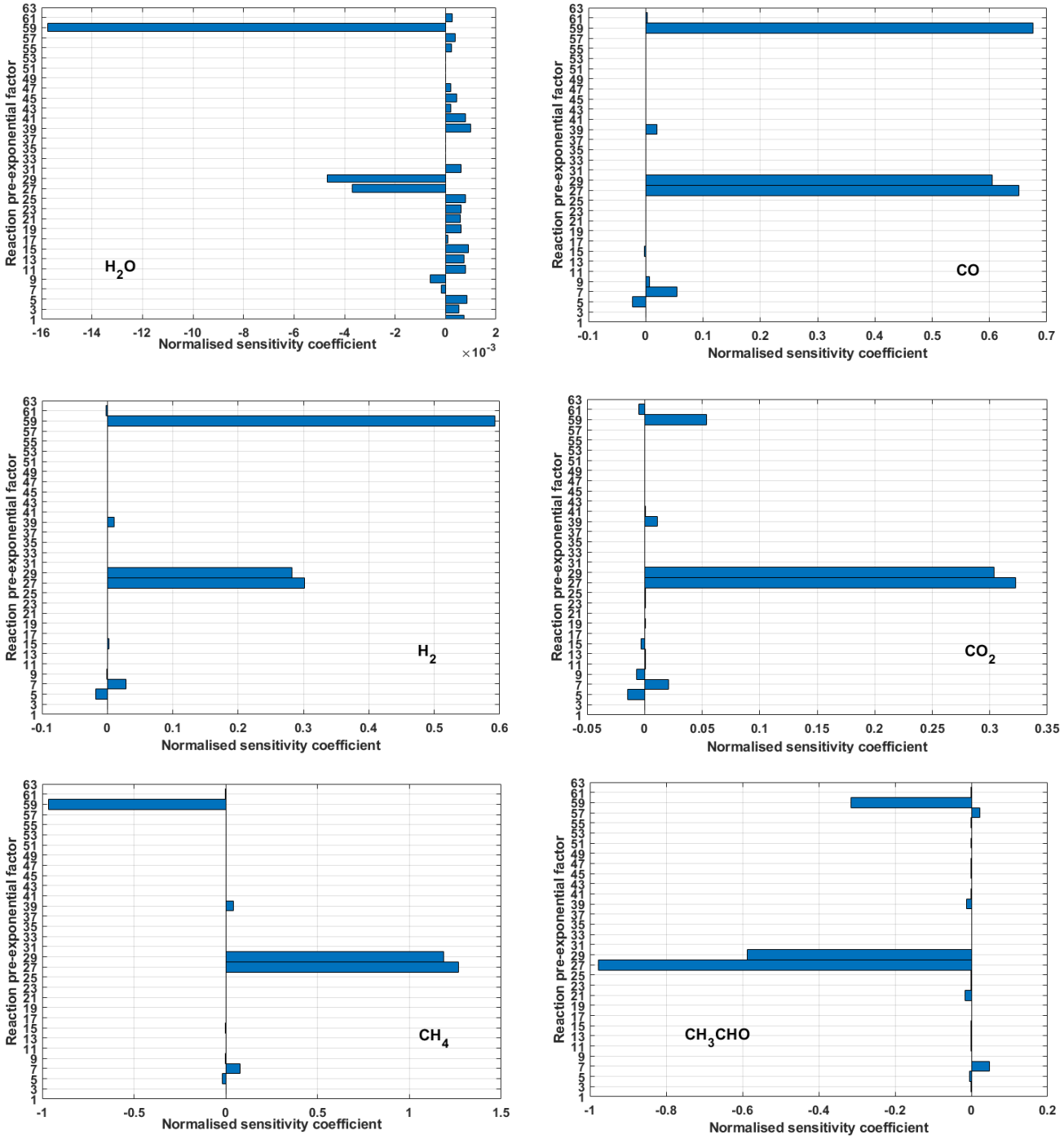

Figure 6. Sensitivity analysis of pre-exponential factors of microkinetic model reactions shown in Table 2 at 400 ^{o}C and $H_2O/C=3$ for products and water outlet molar fractions. Base values for pre-exponential factors are calculated as described in Section 2.2.

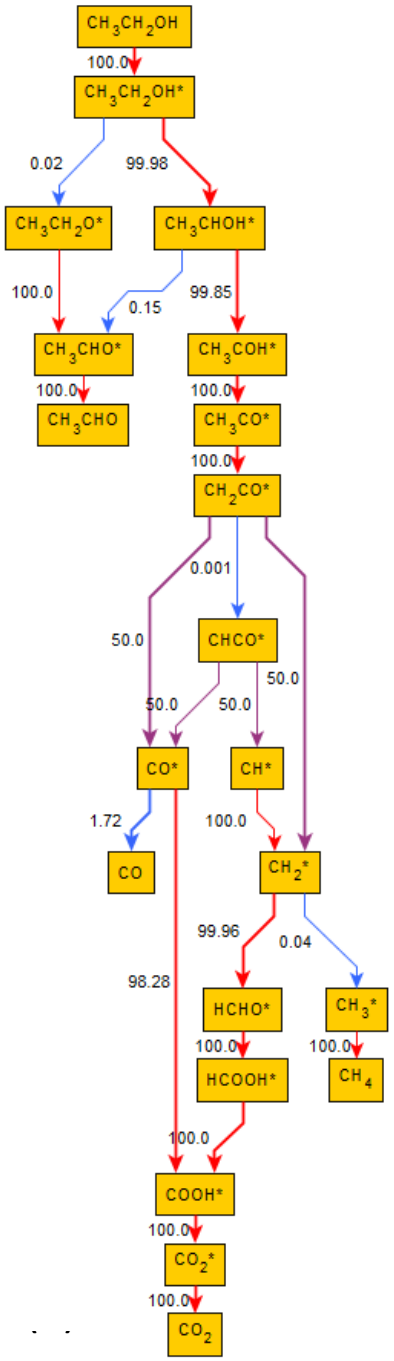

Figure 7. Reaction pathway analysis for ethanol steam reforming over Ni/SiO_2 at 400°C and $H_2O/C=3$ at an ethanol conversion of 25%. Net production rates are considered in calculating contribution percentages of carbon containing species towards other species. Colour mapping from blue to red indicate increasing contribution percentages. Line thickness indicates the relative magnitude of the rates of the reaction.

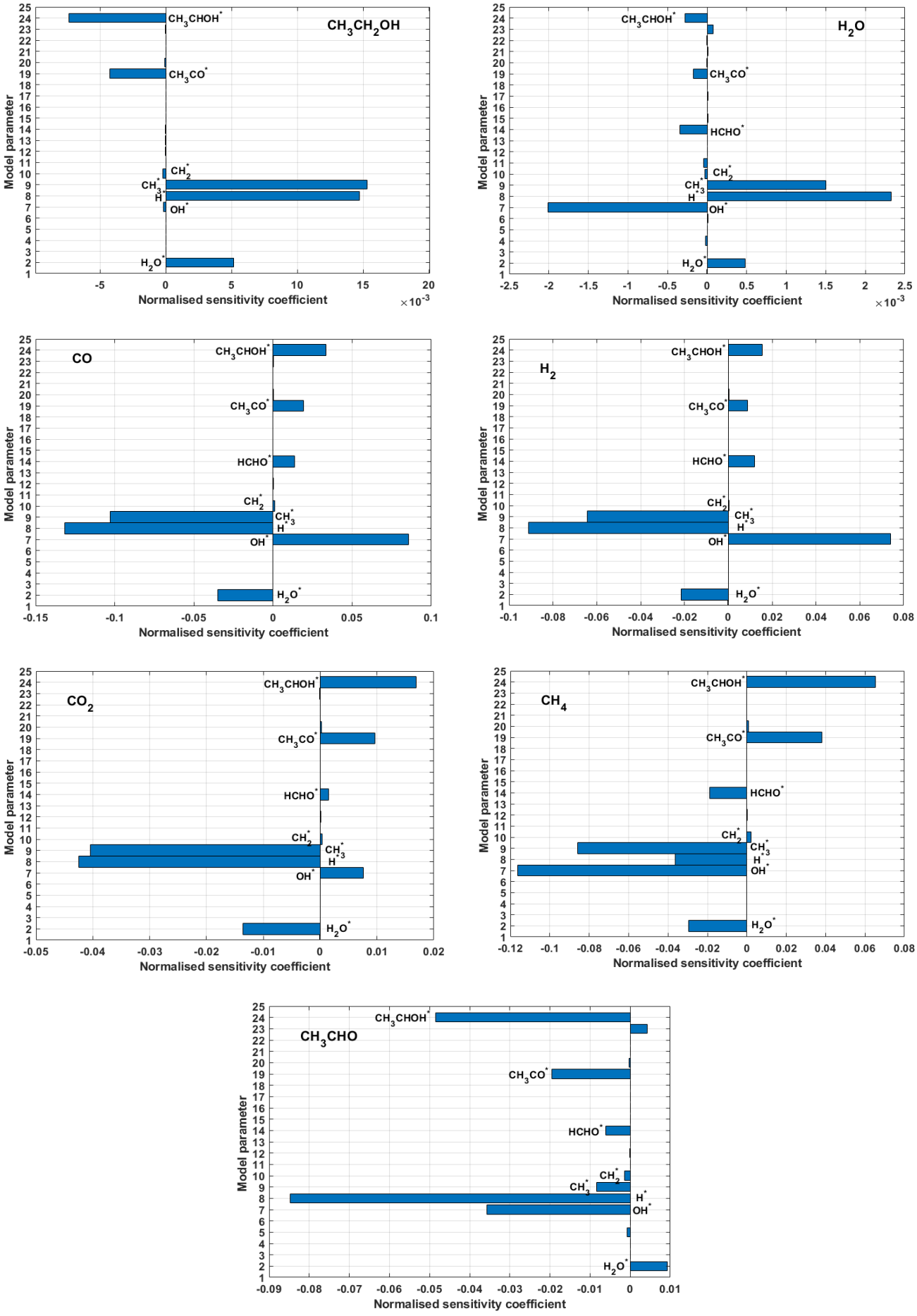

Figure 8. Sensitivity analysis of adsorption enthalpies for liquid and gaseous compounds outlet molar fractions for Ni/SiO_2 at 400°C and $H_2O/C=3$. Base values for model parameters are shown in Table 3.